




ARTICLE

DOI: 10.1038/s41467-017-00467-x

OPEN

Rechargeable aqueous zinc-manganese dioxide batteries with high energy and power densities

Ning Zhang ¹, Fangyi Cheng ^{1,2}, Junxiang Liu¹, Liubin Wang¹, Xinghui Long³, Xiaosong Liu³, Fujun Li ¹ & Jun Chen^{1,2}

Although alkaline zinc-manganese dioxide batteries have dominated the primary battery applications, it is challenging to make them rechargeable. Here we report a high-performance rechargeable zinc-manganese dioxide system with an aqueous mild-acidic zinc triflate electrolyte. We demonstrate that the tunnel structured manganese dioxide polymorphs undergo a phase transition to layered zinc-buserite on first discharging, thus allowing subsequent intercalation of zinc cations in the latter structure. Based on this electrode mechanism, we formulate an aqueous zinc/manganese triflate electrolyte that enables the formation of a protective porous manganese oxide layer. The cathode exhibits a high reversible capacity of 225 mAh g⁻¹ and long-term cyclability with 94% capacity retention over 2000 cycles. Remarkably, the pouch zinc-manganese dioxide battery delivers a total energy density of 75.2 Wh kg⁻¹. As a result of the superior battery performance, the high safety of aqueous electrolyte, the facile cell assembly and the cost benefit of the source materials, this zinc-manganese dioxide system is believed to be promising for large-scale energy storage applications.

¹Key Laboratory of Advanced Energy Materials Chemistry (Ministry of Education) and State Key Laboratory of Elemento-Organic Chemistry, College of Chemistry, Nankai University, Tianjin 300071, China. ²Collaborative Innovation Center of Chemical Science and Engineering, Nankai University, Tianjin 300071, China. ³State Key Laboratory of Functional Materials for Informatics, Shanghai Institute of Microsystem and Information Technology, Chinese Academy of Sciences, Shanghai 200050, China. Correspondence and requests for materials should be addressed to F.C. (email: fycheng@nankai.edu.cn) or to J.C. (email: chenabc@nankai.edu.cn)

There is ever increasing demand of advanced battery technologies with high safety and low cost for applications in portable electronics, electrified vehicles, and renewable energy storage^{1–7}. Although lithium-ion batteries have gained great improvement in energy/power density and life span, the safety issues associated with flammable organic electrolytes and the growing concerns of the price and availability of Li resources impede their large-scale deployment. Battery chemistries based on electrochemical intercalation/storage of Na⁺, K⁺, Mg²⁺, and Zn²⁺ in aqueous electrolytes have been considered as promising alternatives, because of high safety, materials abundance, and environmental friendliness^{8–19}. Rechargeable Zn-ion batteries (ZIBs) are particularly attractive as zinc features higher water compatibility and stability than alkaline metals, allows multi-valent charge transport carriers, and can be produced and recycled with mature industrial process^{20–25}.

Zinc-manganese dioxide (Zn-MnO₂) batteries have dominated the primary battery market because of low cost, high safety, and easy manufacturing^{26–28}. It is highly intriguing to develop rechargeable Zn-MnO₂ batteries. Nevertheless, previous attempts are plagued by poor cycling performance due to the formation of irreversible discharged species (e.g., Mn(OH)₂ and ZnO at cathode and anode, respectively) in alkaline electrolytes^{29–31}. Although alkaline Zn-MnO₂ batteries (Fig. 1a) were shown rechargeable for extended cycles, the delivered capacity is limited at shallow depth of discharge (~10%)³². Recently, the rechargeability of aqueous Zn-MnO₂ batteries has been improved by using mild acidic electrolyte (e.g., aqueous ZnSO₄ solution)^{33–37}. However, the reaction mechanism of MnO₂ polymorphs remains elusive and controversial. For example, electrochemical Zn-insertion in α -MnO₂ is shown to undergo phase transition from tunneled structure to spinel ZnMn₂O₄³³, layered Zn-buserite³⁶, or birnessite³⁸, most of which collapse upon cycling. A different mechanism was referred to the conversion reaction between α -MnO₂ and MnOOH³⁵. For γ -MnO₂, complex multiple-phase transformation was proposed on discharge, involving spinel-type ZnMn₂O₄, tunnel-type γ -Zn_xMnO₂, and layered-type L-Zn_xMnO₂³⁴. Additionally, the Zn-insertion properties in aqueous ZnSO₄ electrolyte are found to vary among polymorphs: α -MnO₂ featuring (2 × 2) + (1 × 1) tunnel structure³⁹ and γ -MnO₂ with (1 × 2) + (1 × 1) tunnels exhibit high capacity (150–300 mAh g⁻¹)^{34, 36}, whereas the most stable (1 × 1) tunneled β -MnO₂ phase^{40, 41} hardly incorporates Zn²⁺ ions³³ due to narrow tunnels⁴². Furthermore, in the widely

investigated ZnSO₄ electrolyte, MnO₂ generally suffers from capacity loss due to the dissolution of Mn²⁺ from Mn³⁺ disproportionation^{34, 35}. Pre-addition of Mn²⁺ salt is proposed to improve capacity retention³⁵ but the underneath mechanism remains unclear. Our previous study indicates that the use of zinc salt with bulky anion (e.g., CF₃SO₃⁻) benefits reactivity and stability of Zn anode and spinel ZnMn₂O₄ cathode²⁴. Therefore, elucidating the electrode reactions of MnO₂ and exploiting compatible electrolyte are desirable in developing rechargeable aqueous Zn-MnO₂ batteries.

Herein, we report high-performance rechargeable aqueous Zn-MnO₂ cells based on MnO₂ cathode, Zn anode, and Zn(CF₃SO₃)₂ electrolyte with Mn(CF₃SO₃)₂ additive. For the widely investigated α -, β -, and γ -MnO₂ polymorphs, we elucidate a common electrode reaction mechanism, by combining electrochemical measurements, X-ray diffraction analysis (XRD), elemental analysis, transmission electron microscopy (TEM), and synchrotron X-ray absorption spectroscopy (XAS). Interestingly, in the exemplified β -MnO₂ that has been previously demonstrated unfavorable for Zn intercalation, a layer-type phase (i.e., Zn-buserite B-Zn_xMnO₂·nH₂O) is generated during the initial discharge, followed by reversible insertion/extraction of Zn²⁺ ions in the layered structure (Fig. 1b). Up to ~0.5 Zn per molecular MnO₂ is accommodated on discharging, along with disproportionated Mn dissolution and capacity fade. We significantly improve the cycling stability of Zn-MnO₂ cell by employing concentrated Zn(CF₃SO₃)₂ electrolyte and Mn(CF₃SO₃)₂ additive (Fig. 1c). The pre-added Mn(CF₃SO₃)₂ is found to suppress Mn²⁺ dissolution and result in the formation of a uniform porous MnO_x nanosheet layer on the cathode surface, which helps to maintain the electrode integrity. Remarkably, β -MnO₂ exhibits high reversible capacity, high rate capability, and stable cyclability. We further demonstrate a soft-packed Zn-MnO₂ full cell that delivers a reversible capacity of 1550 mAh with a total energy density of 75.2 Wh kg⁻¹ after 50 cycles.

Results

Materials synthesis and characterization. We selected pyrolusite β -MnO₂ as a model polymorph, which has been previously demonstrated to exhibit extremely poor electrochemical activity³³ and was prepared by a simple hydrothermal route in this study (detailedly described in experimental section). X-ray diffraction patterns (XRD, Supplementary Fig. 1a) reveals high purity of the

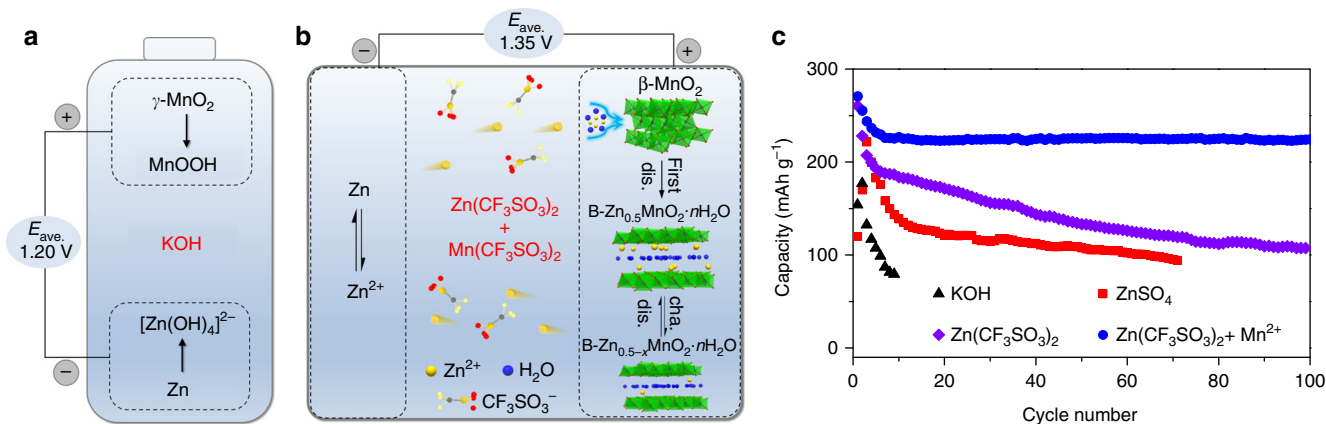


Fig. 1 Zn-MnO₂ battery chemistry. Schematic illustration of **a** the primary alkaline Zn-MnO₂ battery using KOH electrolyte and **b** the rechargeable Zn-MnO₂ cell using CF₃SO₃⁻-based electrolyte. **c** Comparison of the cycling performance of Zn-MnO₂ cells with electrolytes of 45wt.% KOH (at 0.32 C), 3 M ZnSO₄, 3 M Zn(CF₃SO₃)₂, and 3 M Zn(CF₃SO₃)₂ with 0.1 M Mn(CF₃SO₃)₂ additive at 0.65 C. *nC* equals the rate to charge/discharge the theoretical capacity (308 mAh g⁻¹) of MnO₂ in 1/*n* hours

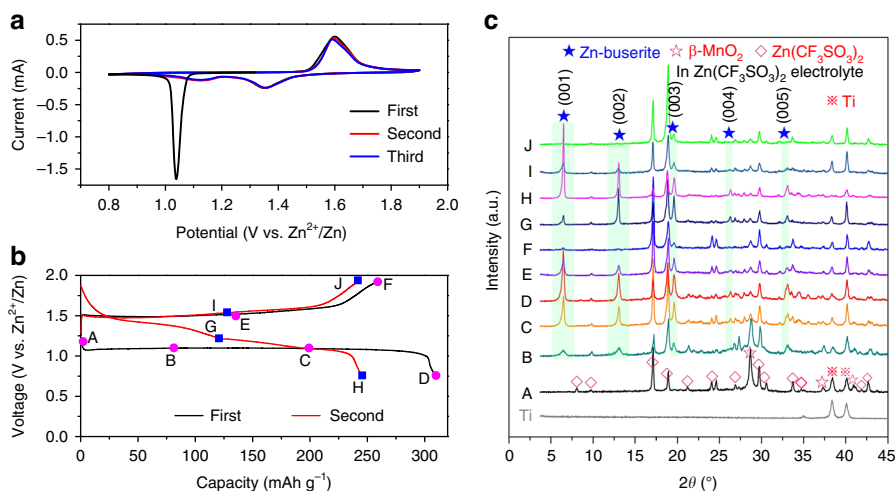


Fig. 2 Electrochemical and structural evolution of β - MnO_2 in Zn-MnO_2 cell. **a** Cyclic voltammograms of β - MnO_2 electrode at a scan rate of 0.1 mV s^{-1} from 0.8 to 1.9 V. **b** Typical charge/discharge curves for the initial two cycles at 0.32 C in 3 M $\text{Zn}(\text{CF}_3\text{SO}_3)_2$ aqueous electrolyte. The points A–J marked the states where data were collected for XRD analysis. **c** XRD patterns of β - MnO_2 electrode at selected states during the first and second cycles

formed tetragonal phase (JCPDS no. 24-735) with P42/mnm space group. Scanning electron microscope (SEM, Supplementary Fig. 1b) of the sample displays nanorod morphology with average length of 2 μm and width of 100–200 nm. Polymorphs of α - MnO_2 and γ - MnO_2 nanorods were also synthesized via hydrothermal technique (Supplementary Fig. 2; Supplementary Methods). Commercial β - MnO_2 powders with large particle size of $\sim 2 \mu\text{m}$ (Supplementary Fig. 3) were employed for comparison.

Electrode reaction mechanism. Figure 2a shows the cyclic voltammograms (CVs) of β - MnO_2 in aqueous 3 M $\text{Zn}(\text{CF}_3\text{SO}_3)_2$ electrolyte. A sharp peak at around 1.06 V is observed during the first cathodic sweeping. In the following cycles, the CV curves are well repeated with two cathodic peaks located at 1.35 and 1.17 V and an overlapped anodic peak at 1.6/1.65 V. The significant difference in CV profiles between the initial and subsequent cycles suggests phase transition. Figure 2b shows the typical galvanostatic profiles of β - MnO_2 at 0.32 C. The first discharge curve displays a flat plateau at around 1.08 V while the second cycle presents two sloping discharge plateaus, in line with the CV results. Notably, the initial discharge capacity reaches 307 mAh g^{-1} , which approaches the theoretical capacity of 308 mAh g^{-1} (based on MnO_2) and corresponds to 0.5 Zn^{2+} per MnO_2 . The evolution of CV profiles and discharge plateaus indicates different mechanism of Zn^{2+} intercalation in MnO_2 electrode^{36, 43}, as discussed below.

To probe the structural evolution of β - MnO_2 in the discharge/charge process, ex-situ XRD patterns (Fig. 2c) were recorded at the selected states (marked points in Fig. 2b). On first discharging (A \rightarrow D), the characteristic peaks of β - MnO_2 are gradually weakened and new phase arises. Besides the peaks designated to the $\text{Zn}(\text{CF}_3\text{SO}_3)_2$ salt, new peaks emerge at 6.47° , 13.00° , 19.58° , 26.28° , and 32.93° , which could be assigned to reflections from the (001)–(005) crystallographic planes of a layered Zn-buserite phase, respectively. The electrolyte salt is precipitated on the surface of both MnO_2 cathode and Zn anode but can be easily removed by immersing and rinsing with water (Supplementary Fig. 4a–c). Notably, the XRD pattern of the rinsed cathode differs from that of previously reported species (e.g., MnOOH ³⁵, spinel ZnMn_2O_4 ³³, birnessite³⁸, tunneled γ - ZnMnO_2 ³⁴, and layered $\text{L-Zn}_x\text{MnO}_2$ ³⁴) in discharged MnO_2 electrodes (Supplementary Fig. 4d). Rietveld refinement of the XRD data of the discharged

electrode suggests the formation of Zn-buserite phase (Supplementary Fig. 4e). The exact structural motif of Zn-buserite is not determined yet, but will be further investigated in the future. The Zn-buserite phase, commonly found in layered Mn oxide mineral^{44–46}, contains H_2O layers in the channels between two MnO_6 octahedron slabs (Fig. 1b), featuring a similar structure with Ca-buserite⁴⁴ (JCPDS No.50-0015). Zn^{2+} cations reside above and below the Mn vacant sites and are coordinated with three O atoms adjacent to the vacancies and three O atoms from interlayer H_2O ^{36, 44–46}. The presence of H_2O in the discharged species was validated using thermal gravimetric analysis (TGA), indicating a composition of ~ 2.28 molecular H_2O per formula of Zn-buserite (Supplementary Fig. 5). In the followed charging process (D \rightarrow F), the intensity of characteristic peaks for the layered phase was gradually weakened upon extraction of Zn ions. This peak attenuation could be explained by the decrease of scattering atom concentration in unit cell and the weakening of Zn–O interaction due to Zn egress. Similar intensity variation of (00l) reflection has been observed on layered intercalation electrodes such as vanadium oxides^{9, 47}. In the second cycle, the signals of layered compound were reversibly strengthened/weakened upon Zn^{2+} insertion/extraction. The presence of β - MnO_2 can be observed in the initial several cycles but is not discernable after 10 cycles (Supplementary Fig. 6). We investigated the structural evolution of α - MnO_2 and γ - MnO_2 cathodes as well. Interestingly, these two polymorphs undergo phase transformation to layered Zn-buserite upon first discharging and reversible Zn intercalation in the layered structure on subsequent cycling (Supplementary Figs. 7 and 8), resembling the case of β - MnO_2 . The results suggest common electrode reaction mechanism in tunneled polymorphs of MnO_2 , which to the best of our knowledge, is first elucidated in mild acidic electrolytes.

The structural evolution of β - MnO_2 electrode was further investigated by ex-situ TEM analysis. Figure 3a, b displays the TEM and high-resolution TEM (HRTEM) images at the initial state, where the lattice fringes can be indexed to the (110) plane of β - MnO_2 . The annular bright field-scanning TEM (ABF-STEM) image (Fig. 3c) clearly shows the atomic arrangement within the tunnel-like framework, as schematically viewed along the [100] direction of the lattice (Fig. 3d). After fully discharging, the one-dimensional nanorod shape is maintained, while the surface of electrode becomes rough with the formation of aggregated nanoparticles (Fig. 3e), which is ascribed to the structural

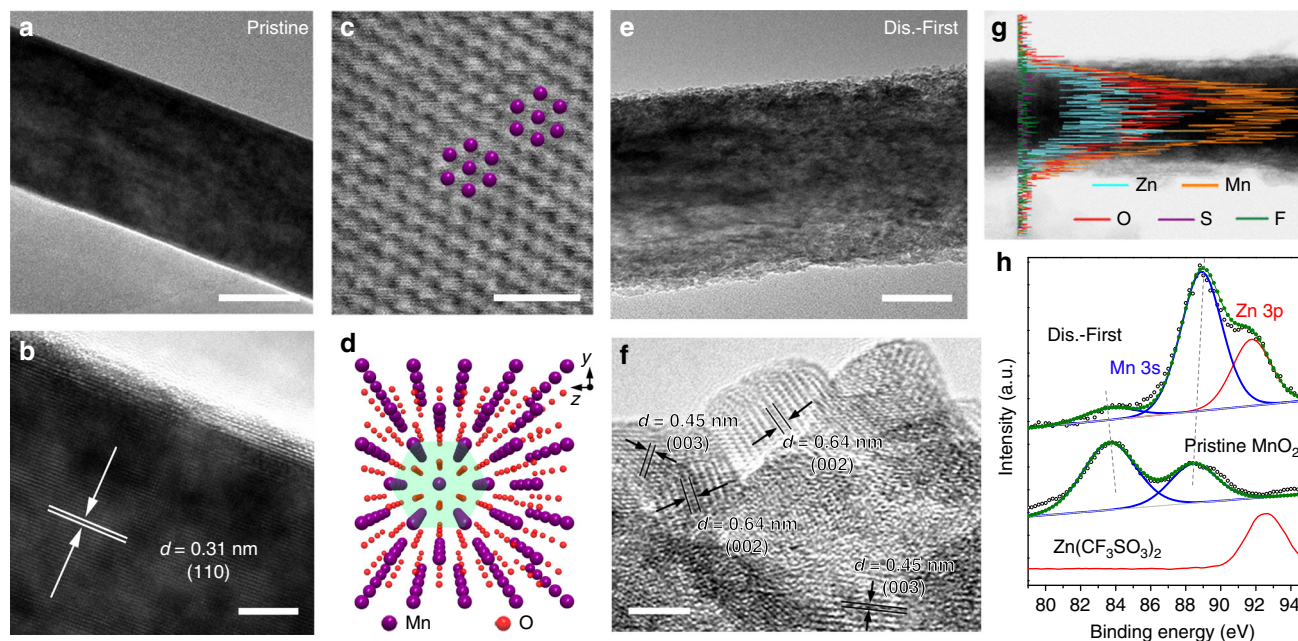


Fig. 3 Microstructural and compositional analysis of MnO_2 . **a** TEM image, **b** HRTEM image, **c** ABF-STEM image, and **d** schematic atomic model (viewed from the $[100]$ zone axis) at the initial state. **e** TEM image, **f** HRTEM image, **g** EDS line scanning profiles in TEM, and **h** XPS spectra of the first fully discharged electrode. Scale bars, 50 nm **a**, **e**; 5 nm **b**, **f**; and 1 nm **c**, respectively

distortion in the phase-conversion process. The observed lattice fringes with interplanar distances of 0.45, 0.64, and 1.29 nm correspond to the (003), (002), and (001) planes of Zn-buserite (Fig. 3f and Supplementary Fig. 9a), respectively, consistent with the XRD analysis.

To eliminate the impact of precipitated electrolyte salt, the discharged electrode was rinsed with water for elemental dispersive spectroscopy (EDS) and X-ray photoelectron spectroscopy (XPS) analysis. The line scanning profile in TEM (Fig. 3g) and elemental mapping (Supplementary Fig. 9b) in STEM of the discharged electrode reveal the uniform distribution of Zn, Mn and O, whereas S and F from electrolyte are not detectable (Fig. 3g). In XPS spectra, the energy splitting (ΔE) of Mn 3s doublet peaks is 4.7 and 5.0 eV for pristine and discharged electrodes, respectively, indicating reduced Mn valence after Zn insertion (Fig. 3h). At discharged state, a new Zn 3p peak appears at 92.0 eV, which is lower than that of $\text{Zn}(\text{CF}_3\text{SO}_3)_2$ (92.7 eV) and could be assigned to the intercalated Zn. These results confirm the presence of Zn^{2+} ions into the layered manganese oxide host and rule out the possibility of electrode reactions associated with CF_3SO_3^- anions. Furthermore, the TEM images of $\beta\text{-MnO}_2$ electrode after different cycles (Supplementary Fig. 10) indicate expansion and exfoliation of nanorods, which is attributed to the phase transition, Mn dissolution and repeated Zn^{2+} intercalation, and would incur capacity loss during cycling.

To gain insight into the variation of Mn oxidation state and electronic structure during the (de)intercalation process, we performed the synchrotron XAS characterization, which has been demonstrated useful to analyze manganese oxides^{48–52}. Figure 4a shows the normalized Mn K-edge XANES (X-ray near edge absorption structure) profiles of $\beta\text{-MnO}_2$ electrode at selected states in the initial two cycles. The nominal Mn valence was plotted vs. excitation energy of reference manganese oxides to establish fitted linear correlation (Fig. 4b). On discharging, the entire edge shifts toward lower energy, indicating a decrease of the average Mn oxidation state. The mean Mn valence at fully discharged state is estimated to be 3.6. During first charging, the edge position slightly shifts back to higher energy, while it remains almost unchanged in the second cycle. The interesting

point is that the Mn valence should increase/decrease with Zn^{2+} intercalation/deintercalation and would approach 3 for the fully discharged electrode, as anticipated from the discharged capacity (Fig. 2b). We postulate that such unexpected observation could be ascribed to the disproportionational dissolution of trivalent Mn species ($\text{Mn}^{3+}_s \rightarrow \text{Mn}^{4+}_s + \text{Mn}^{2+}_{\text{aq}}$)^{38, 53}. Analysis of Mn by inductively coupled plasma atomic emission spectrometer (ICP-AES) evidences the change of Mn concentration in the electrolyte (Supplementary Fig. 11; Supplementary Note 1). On discharging, the amount of dissolved Mn increases and corresponds to $\sim 8.9\%$ of the total manganese at full discharge. The partial dissolution of Mn in electrolyte is a feasible attribution to the noticeable capacity loss on cycling.

Figure 4c shows the EXAFS (extended X-ray absorption fine structure) spectra of $\beta\text{-MnO}_2$ electrode at selected Zn (de) intercalation stages. The strongest peak located at 1.5 Å is attributed to the closest oxygen (Mn-O) in the MnO_6 octahedra. The peaks at 2.5 and 3.0 Å are assigned to Mn in the edge-sharing (Mn-Mn_{edge}) and corner-sharing (Mn-Mn_{corner}) MnO_6 octahedra (Fig. 4d), respectively^{51, 54}. When the electrode was fully discharged, the relative intensity of the Mn-Mn_{corner} peak decreased to a much larger extent than that of Mn-O and Mn-Mn_{edge} signals (Supplementary Fig. 12). This result is indicative of the breakage of the corner-shared MnO_6 octahedra. Furthermore, the 3.0 Å peak broadens and slightly shifts to larger distance, which is related to the formation of Mn-O-Zn energy-absorbing path between the layered MnO_6 octahedron slabs and inserted Zn ions. A comparison of the crystallographic structure between $\beta\text{-MnO}_2$ and Zn-buserite suggests that the co-insertion of Zn^{2+} and H_2O and the dissolution of Mn distort the pyrolusite framework, leaving Mn vacancies in the upper/underlying layers and generating layered Zn-buserite. This tunnel-to-layer phase transition is irreversible, as indicated by the absence of EXAFS spectra recovery on first recharge. Meanwhile, the broadened 3.0 Å peak is not fully recovered after second charging, which can be attributed to the capacity loss (Fig. 2b). Notably, XAS analysis of $\alpha\text{-MnO}_2$ and $\gamma\text{-MnO}_2$ electrodes (Supplementary Fig. 13) reveals similar behavior with that of $\beta\text{-MnO}_2$, again suggesting common electrode reaction mechanism among different tunneled MnO_2 polymorphs.

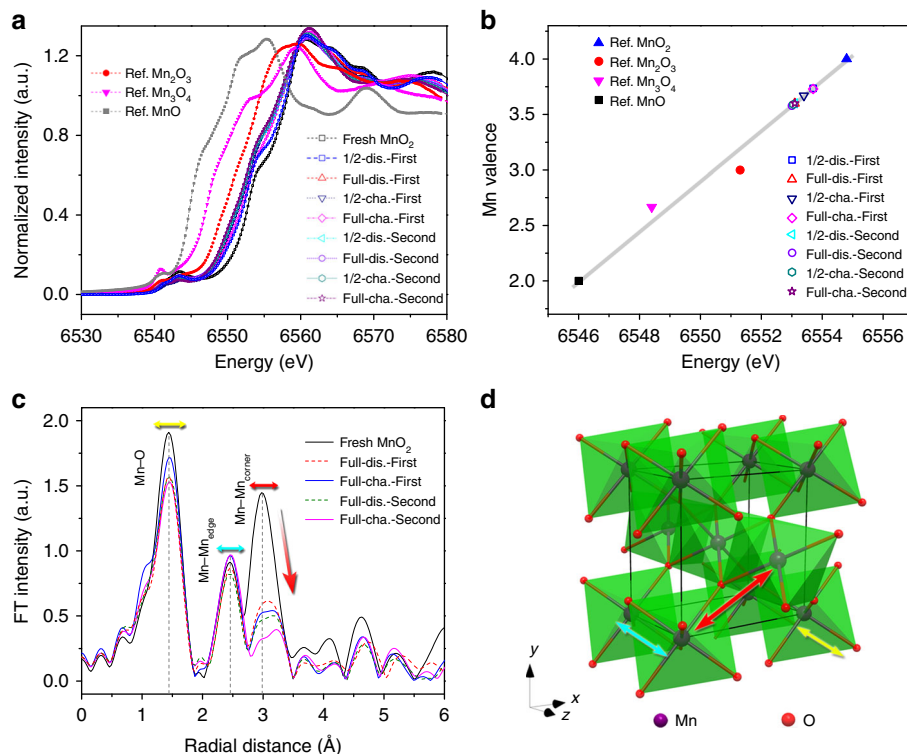


Fig. 4 XAS characterization of β -MnO₂ electrode. **a** Mn-K edge XANES curves at selected discharge/charge states, with reference to standard MnO, Mn₂O₃, and Mn₃O₄. **b** Fitted linear relationship between the photon energy and oxidation state of Mn element. **c** The EXAFS spectra. **d** Schematic depiction of the unit cell of β -MnO₂

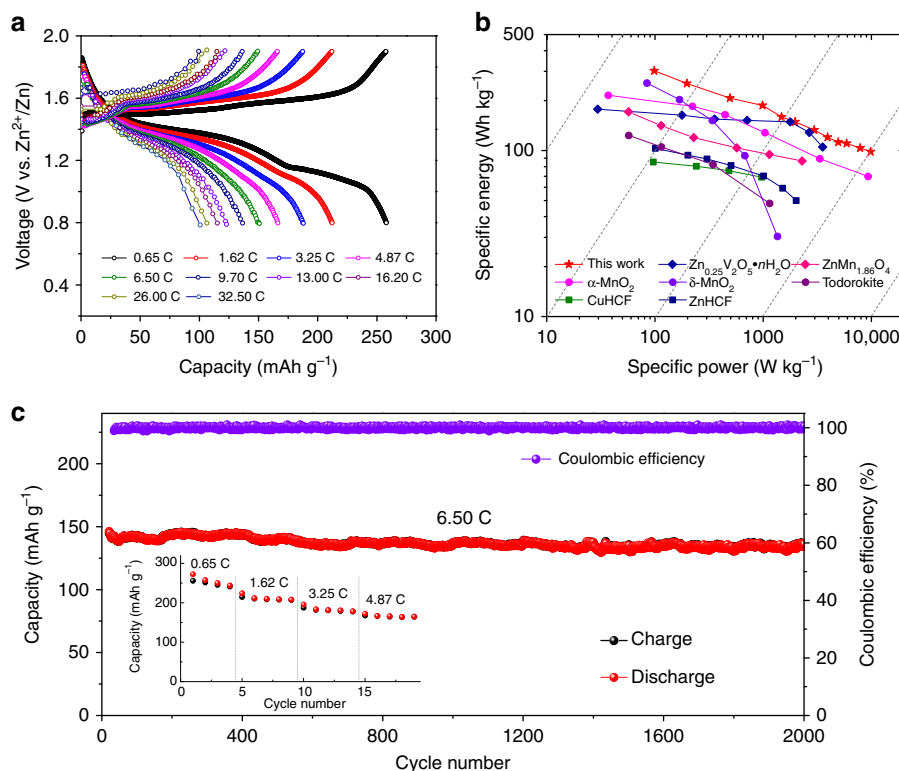


Fig. 5 Electrochemical performance of Zn-MnO₂ cells in 3 M Zn(CF₃SO₃)₂ electrolyte with 0.1 M Mn(CF₃SO₃)₂ additive. **a** Discharge/charge profiles at varying C rates. **b** The Ragone plots of Zn-MnO₂ battery and ZIBs with other reported cathode materials. Values are based on the total active mass of both cathode and anode. **c** Long-cycle performance at rate of 6.5 C. Inset shows the capacity evolution at the initial 19 cycles

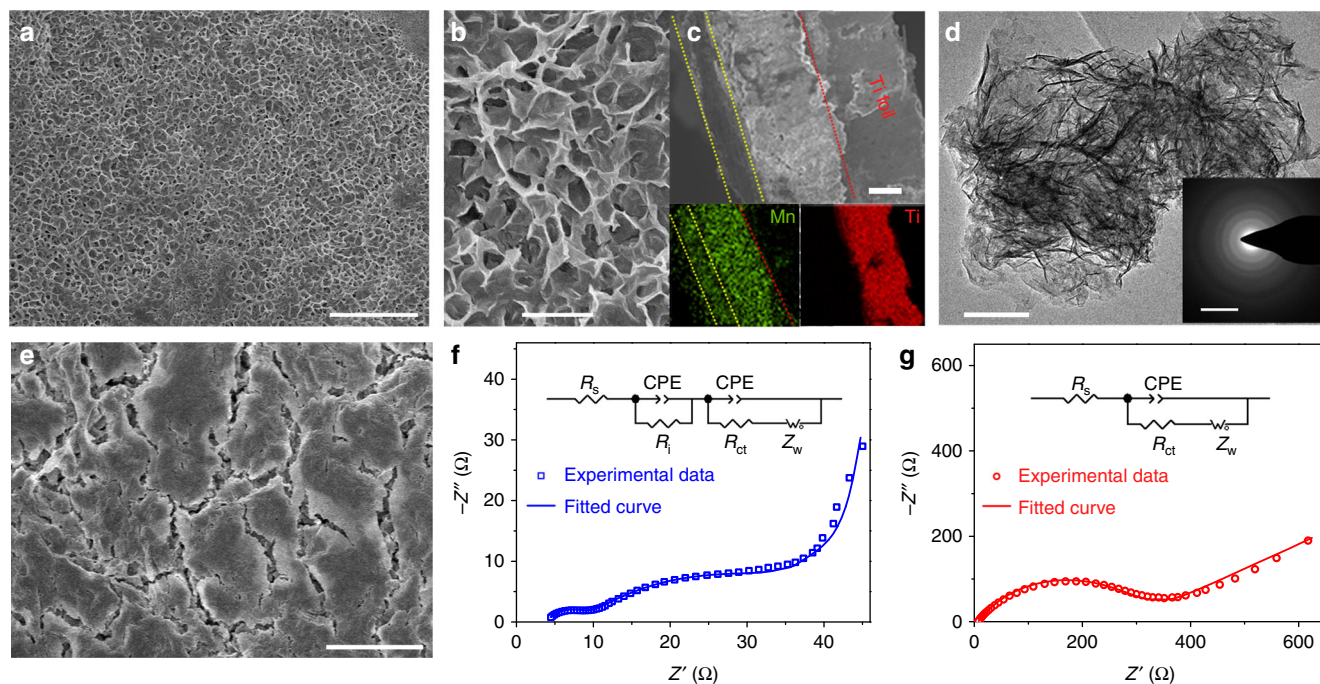


Fig. 6 Function of pre-added Mn^{2+} in electrolyte. **a, b, c, e** SEM, **d** TEM images, and **f, g** three-electrode-cell EIS analysis of re-obtained cathodes after ten cycles in 3 M $\text{Zn}(\text{CF}_3\text{SO}_3)_2$ electrolyte **a-d, f** with and **e, g** without 0.1 M $\text{Mn}(\text{CF}_3\text{SO}_3)_2$ additive. Insets of **c, d** show elemental mapping and SAED pattern, respectively. Insets of **f, g** show the equivalent circuit to fit the EIS data, where R_s , R_i , R_{ct} , CPE, and Z_w represent series resistance, interface resistance between electrolyte and deposited layer, charge-transfer resistance, constant-phase element, and Warburg diffusion process, respectively. Scale bars, 5 μm **a, e**; 1 μm **b**; 10 μm **c**; 100 nm **d**; and 5 1/nm (inset of **d**), respectively

Electrochemical performance. To evaluate the electrochemical performance, coin-type Zn-MnO₂ cell was assembled in ambient air by using β -MnO₂ nanorod cathode, Zn foil anode, filter paper separator, and aqueous $\text{Zn}(\text{CF}_3\text{SO}_3)_2$ electrolyte. The concentrated 3 M $\text{Zn}(\text{CF}_3\text{SO}_3)_2$ results in better cyclic stability than diluted electrolyte (e.g., 1 M) (Supplementary Fig. 14), which is ascribed to the decrease of water activity and water-induced side reactions^{4, 24, 55}. As shown in Fig. 1c, the cells based on mild acidic electrolyte (3 M ZnSO_4 , pH ~ 3.4; 3 M $\text{Zn}(\text{CF}_3\text{SO}_3)_2$, pH ~ 3.6) show much better cycling performance as compared with that employing KOH electrolyte. Meanwhile, the cell using $\text{Zn}(\text{CF}_3\text{SO}_3)_2$ electrolyte delivers much higher initial discharge capacity than that of ZnSO_4 (275 vs. 120 mAh g^{-1}) at 0.65 C. However, similar capacity deterioration is observed upon cycling, due to the loss of active mass. To address this issue, we pre-added Mn^{2+} salts into the electrolyte to accommodate the dissolution equilibrium of Mn^{2+} from MnO₂ electrode. By eliminating the anion effect, we selected $\text{Mn}(\text{CF}_3\text{SO}_3)_2$ as the electrolyte additive, with concentration from diluted 0.01 M to the saturated 0.1 M. The optimized electrolyte composition was found to be 3 M $\text{Zn}(\text{CF}_3\text{SO}_3)_2 + 0.1$ M $\text{Mn}(\text{CF}_3\text{SO}_3)_2$, which results in the highest Coulombic efficiency and ionic conductivity as well as high capacity of 225 mAh g^{-1} after 100 cycles (Supplementary Figs. 15 and 16).

Figure 5a shows the charge/discharge profiles of Zn-MnO₂ cells at different current densities. Discharge capacities of 258, 213, 188, 151, and 115 mAh g^{-1} were recorded at rates of 0.65, 1.62, 3.25, 6.50, and 16.20 C, respectively. Even at a high rate of 32.50 C, a reversible capacity of 100 mAh g^{-1} could be obtained. In addition, when the rate shifted back to 0.65 C, the capacity recovered to 246 mAh g^{-1} , showing a strong tolerance to the rapid Zn^{2+} ions insertion/extraction (Supplementary Fig. 17). The superior rate performance can be further viewed from the Ragone plots (specific energy vs. specific power) by comparing the Zn-MnO₂ system to reported α -MnO₂³³, δ -MnO₂⁵⁶,

$\text{Zn}_{0.25}\text{V}_2\text{O}_5 \cdot n\text{H}_2\text{O}$ ⁹, $\text{Zn}_{1.86}\text{Mn}_2\text{O}_4$ ²⁴, todorokite³⁷, $\text{KCuFe}(\text{CN})_6$ (CuHCF)²¹, and $\text{Zn}_3[\text{Fe}(\text{CN})_6]_2$ (ZnHCF)⁵⁷ cathodes for aqueous ZIBs (Fig. 5b). High-specific energy and specific power (254 Wh kg^{-1} at 197 W kg^{-1} ; 110 Wh kg^{-1} at 5910 W kg^{-1}) can be simultaneously achieved, which is promising for energy storage applications. The Zn-MnO₂ cell was galvanostatically discharged/charged at 6.50 C (Fig. 5c) to evaluate the long-term cycling stability. Remarkably, the reversible capacity sustains 135 mAh g^{-1} with a capacity retention of 94% over 2000 cycles and Coulombic efficiency approaching 100%.

We also investigated the Zn-MnO₂ cells with 3 M $\text{ZnSO}_4 + 0.1$ M MnSO_4 and 3 M $\text{Zn}(\text{CF}_3\text{SO}_3)_2 + 0.1$ M MnSO_4 electrolytes, which delivered initial discharge capacity of 110 and 205 mAh g^{-1} , respectively (Supplementary Fig. 18). In SO_4^{2-} -based electrolyte, an increase of capacity was observed within the first several cycles, which was attributed to the activation process that has been similarly found in reported α -/ γ -MnO₂ cathodes³⁴⁻³⁶. Interestingly, the CF_3SO_3^- -based electrolyte endows much higher initial discharge capacity (275 mAh g^{-1} at 0.65 C) and results in capacity stabilization after ~ 10 cycles. The different behaviors could be ascribed to the $\text{Zn}(\text{CF}_3\text{SO}_3)_2$ solution that not only features higher ionic conductivity (Supplementary Fig. 19) but also enables faster kinetics and higher stability of Zn plating/stripping as compared with sulfate and alkaline electrolytes (Supplementary Fig. 20; Supplementary Note 2). Besides, the bulky CF_3SO_3^- anion (vs. SO_4^{2-} with double charge) could decrease the number of water molecules surrounding Zn^{2+} cations and reduce the solvation effect²⁴, thus facilitating Zn^{2+} ions transportation and charge transfer.

Although the pre-addition of Mn^{2+} in electrolyte has been demonstrated to enhance the cyclability of MnO₂ electrode³⁵, the underneath mechanism remains unclear. To further understand the functions of pre-added Mn^{2+} , we have carried out a series of analytical studies, including electrochemical measurements, XRD, Raman, XPS, XANES, and SEM/TEM. In acidic electrolyte, manganese oxides (MnO_x) such as MnO₂ or Mn₂O₃ can be

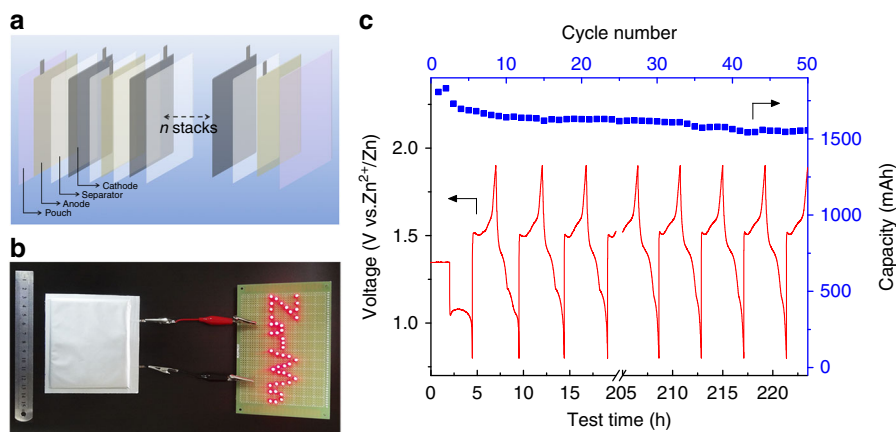
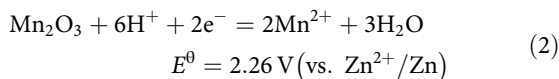
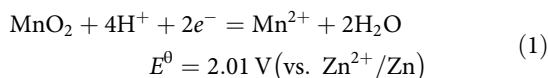


Fig. 7 Electrochemical performance of pouch-type Zn-MnO₂ battery. **a** Schematic illustration of the cell configuration with anode—separator—cathode stacks. **b** A digital photo of the soft-package battery powering a series of LED lights. **c** Cycling performance in the voltage range of 0.8–1.9 V at constant current of 0.72 A

generated from electrolysis of Mn²⁺-containing solution³² based on the following reactions:



According to Nernst equation, the required theoretical potentials to form MnO₂ and Mn₂O₃ in Mn(CF₃SO₃)₂ (0.1 M, pH 6.0) solution are 1.35 and 1.26 V (vs. Zn²⁺/Zn), respectively; the corresponding values are 1.60 and 1.64 V in 3 M Zn(CF₃SO₃)₂ electrolyte containing 0.1 M Mn²⁺ (pH 3.8). This estimation is consistent with the voltammetry results of three-electrode measurements (Supplementary Fig. 21; Supplementary Note 3), which also reveals that Mn²⁺ is not reduced within the investigated potential windows. After charging in 3 M Zn(CF₃SO₃)₂ + 0.1 M Mn(CF₃SO₃)₂ electrolyte, brown deposit layer was observed on the electrode. The layer is composed of manganese oxide with Mn oxidation state between +3 and +4, and features nanosheet morphology and poor crystallinity, as analyzed by SEM, XRD, Raman, XPS, and XAENS (Supplementary Fig. 22).

In post-mortem analysis of Zn-MnO₂ cell using 3 M Zn(CF₃SO₃)₂ + 0.1 M Mn(CF₃SO₃)₂ electrolyte, we also observed an interconnected porous MnO_x layer on the cathode surface after charging (Fig. 6a, b). The cross-sectional SEM image and elemental mapping images (Fig. 6c) evidence the presence of a uniform layer with thickness around 10 μm. TEM imaging and selected area electron diffraction (SAED) analysis reveal porous nanosheet microstructure and amorphous character of the deposited layer (Fig. 6d), which would facilitate mass diffusion. In contrast, the integrity of β-MnO₂ electrode was seriously destroyed with the formation of cracks in 3 M Zn(CF₃SO₃)₂ electrolyte without Mn(CF₃SO₃)₂ additive (Fig. 6e). The electrode pulverization would break the electronic conducting network and increase electrode polarization, further aggravating the capacity decay. Electrochemical impedance spectroscopy (EIS) was performed in a three-electrode cell, using the dismantled cathode after ten cycles as the working electrode, platinum plate as the counter electrode, and saturated calomel electrode (SCE) as the reference electrode. The cycled electrode in Mn²⁺-added electrolyte displays two depressed semicircles in high frequency area and one line in low frequency region (Fig. 6f). Fitting the EIS data

(Supplementary Table 1) gives a series resistance (*R_s*, 4.5 Ω), an interface resistance (*R_i*, 6.0 Ω) between electrolyte and deposited layer, a charge-transfer resistance (*R_{ct}*, 25 Ω) and a Warburg diffusion impedance (*Z_w*, 124.7 Ω). In comparison, the cell without electrolyte additive shows higher *R_s* (8.0 Ω), *R_{ct}* (350 Ω), and *Z_w* (1200 Ω), in the absence of the apparent interface component (Fig. 6g).

Based on the above results, we propose three merits of the Mn²⁺ electrolyte additive for the Zn-MnO₂ battery: (1) accommodating and compensating Mn²⁺ dissolution from the electrode, (2) improving initial Coulombic efficiency and ionic conductivity of the electrolyte and (3) generating a uniform porous nanostructured MnO_x film on the cathode surface, which helps to maintain the electrode integrity and favor charge transfer. Note that the generated MnO_x layer itself contributes to nearly 2.4% of the capacity delivered by the active material (Supplementary Fig. 23). The Zn(CF₃SO₃)₂ + Mn(CF₃SO₃)₂ electrolyte is also applicable to improve the cycling stability of nanostructured α-MnO₂ and γ-MnO₂ cathodes (Supplementary Fig. 24a, b). Furthermore, commercial β-MnO₂ powders with irregular shape and micrometer particle size (Supplementary Fig. 3) also exhibit considerable capacity (132 mAh g⁻¹ at 0.65 C) and cyclability (200 cycles) in this electrolyte (Supplementary Fig. 24c, d).

The Zn anode was also investigated to understand the high-performing Zn-MnO₂ cell chemistry (Supplementary Figs. 25–28). Post-mortem analysis of cycled Zn in three-electrode cell with 3 M Zn(CF₃SO₃)₂ + 0.1 M Mn(CF₃SO₃)₂ electrolyte reveals a dense and dendrite-free surface morphology after 280 h of repeated Zn plating/stripping (Supplementary Fig. 25). In a Zn-MnO₂ full cell, neither dendritic morphology nor formation of byproducts such as ZnO or Zn(OH)₂ was evidenced after rate test (Supplementary Fig. 26), favoring the cyclic stability of Zn-MnO₂ batteries. In contrast, in 3 M ZnSO₄ + 0.1 M MnSO₄ electrolyte, Zn plate with lots of cracks formed on the zinc surface, while ZnO nanorods were observed in KOH electrolyte, which would deter the cyclability of Zn (Supplementary Figs. 25 and 27). Furthermore, the EDS analysis indicates that there is no detectable Mn in Zn anode (Supplementary Fig. 28).

Discussion

The exceptional performance of Zn-MnO₂ coin-type batteries has motivated us to further assess soft-packed full cells, which were facilely assembled in ambient air negating complicated

procedures or extra protection (Supplementary Methods). Figure 7a schematically shows the battery configuration consisting of six anode–separator–cathode stacks. A typical assembled pouch-type cell lightens a “Zn–Mn”–shape indicator containing 44 LEDs (Fig. 7b). A stable discharge capacity of 1550 mAh can be obtained after 50 repeated cycles with an average potential of 1.35 V (Fig. 7c). The full cell delivers an energy density of 158.5 Wh kg⁻¹ based on the total weight of the active materials (including both cathode and anode). This value far exceeds that of other aqueous Li-ion batteries (50–90 Wh kg⁻¹)^{3, 4, 58} and aqueous Na-ion batteries (~33 Wh kg⁻¹)^{8, 16, 59}. Remarkably, a total energy density of 75.2 Wh kg⁻¹ is obtained according to the mass of whole battery mass, much higher than that of commercial Pb-acid (~30 Wh kg⁻¹) and Ni–Cd technologies (~50 Wh kg⁻¹)²⁶. We note that the higher price of anhydrous Zn(CF₃SO₃)₂ salt relative to ZnSO₄ and KOH would inevitably increase the practical cost of this aqueous Zn–MnO₂ battery system, even though Zn(CF₃SO₃)₂ merely serves as charge carrier and is not consumed during battery operation. Fortunately, considering the abundant, cheap precursors (i.e., triflic acid and ZnCO₃)⁶⁰ and the direct usage of hydrate-form salt in aqueous solution, the cost of Zn(CF₃SO₃)₂ electrolyte could be expected to drop with the development of synthetic technique and market demand.

In conclusion, we demonstrate a high-performing rechargeable Zn–MnO₂ battery system based on zinc anode, β–MnO₂ cathode, and mild acidic aqueous electrolyte. We elucidate the Zn-insertion mechanism and structural evolution of MnO₂ cathode by combining electrochemical investigations, XRD, TEM, ICP, and XANES/EXAFS analysis. A phase transition from tunneled to layered structure (Zn–buserite) occurs during the first discharge of MnO₂, followed by reversible Zn²⁺ (de)intercalation in the H₂O-containing Zn–buserite framework. Unlike previous reports, this electrode mechanism is common in polymorphs of α–MnO₂, γ–MnO₂, and β–MnO₂. The phase transformation, Mn dissolution and electrode pulverization incur capacity fade of MnO₂. By formulating an aqueous 3 M Zn(CF₃SO₃)₂ + 0.1 M Mn(CF₃SO₃)₂ electrolyte, the Mn²⁺ dissolution can be effectively accommodated and the electrode integrity can be maintained because of the in-situ generated amorphous MnO_x layer. As a result, Zn–MnO₂ cell exhibits high capacity (225 mAh g⁻¹ at 0.65 C), high rate capability (100 mAh g⁻¹ at 32.50 C) and long-term cycling stability (94% capacity retention after 2000 cycles at 6.50 C). Furthermore, the assembled soft-packed Zn–MnO₂ battery can deliver a high reversible capacity of 1550 mAh with a total energy density of 75.2 Wh kg⁻¹, among the highest value achieved in aqueous battery technologies. The present Zn–MnO₂ system holds great promise for potential applications in large-scale energy storage, in view of the remarkable electrochemical performance and other advantages such as low materials cost, easy manufacturing, high safety, and environmental friendliness.

Methods

Synthesis. β–MnO₂ nanorods were synthesized by a hydrothermal method. In a typical synthesis, 30 ml KMnO₄ (0.1 M) and 30 ml MnSO₄·H₂O (0.6 M) were mixed under continuous stirring for 30 min at room temperature. The mixture was loaded into a 100 ml Teflon-lined autoclave and maintained at 140 °C for 12 h. The obtained product was centrifuged, washed thoroughly using water and absolute ethyl alcohol, and dried at 80 °C for 10 h. Bulk β–MnO₂ powders was purchased from Alfa Aesar. α–MnO₂ and γ–MnO₂ nanorods were synthesized via hydrothermal technique following previously reported procedures⁶¹.

Characterization. Powder XRD patterns were collected on a Rigaku X-ray diffractometer (MiniFlex600) with Cu Kα radiation. SEM images were obtained on Field-emission JEOL JSM-7500F microscope. TEM and HRTEM images were taken on Philips Tecnai G2 F20. ABF-STEM was performed on Titan Cubed Themis G2 300 (FEI) at an acceleration voltage of 200 kV. The XAS data were collected on BL14W1 beamline of Shanghai Synchrotron Radiation Facility and

analyzed with software of Iffeffit Athena⁶². ICP–AES measurements were conducted on a PerkinElmer Optima 8300. XPS was tested on a Perkin Elmer PHI 1600 ESCA system. Raman spectra were obtained on confocal Thermo–Fisher Scientific DXR microscope using 532 nm excitation. TGA was measured by a Netzsch STA 449 F3 Jupiter analyzer.

Electrochemical test. Electrochemical performance was tested using CR2032 coin-type cells. The working electrode was fabricated by blending MnO₂ powder, Super P carbon and polyvinylidene fluoride in a weight ratio of 8:1:1 using *N*-methyl-2-pyrrolidone as solvent. The obtained slurry was pasted onto a Ti foil and vacuum-dried at 100 °C for 12 h. The loading mass of active material was ~2 mg cm⁻². Filter paper and zinc foil were employed as the separator and anode, respectively. A 3 M Zn(CF₃SO₃)₂ with/without 0.1 M Mn(CF₃SO₃)₂ aqueous solution was used as the electrolyte. The assembled cells were galvanostatically cycled between 0.8 and 1.9 V using the LAND-CT2001A battery-testing instrument. Calculation of specific capacities was based on the mass of initial MnO₂. CVs were measured on a Parstat 263 A electrochemical workstation (AMETEK). EIS was performed on a Parstat 2273 electrochemical workstation (AMETEK). The AC perturbation signal was ±10 mV and the frequency ranged from 100 kHz to 100 mHz. The electrochemical behaviors of Mn²⁺ additive in electrolyte were characterized using three-electrode cells (Ti foil as working electrode, platinum plate or Zn foil as counter electrode, and SCE as reference electrode).

Data availability. The authors declare that all the relevant data are available within the paper and its Supplementary Information file or from the corresponding author upon reasonable request.

Received: 6 January 2017 Accepted: 27 June 2017

Published online: 01 September 2017

References

- Armand, M. & Tarascon, J. M. Building better batteries. *Nature* **451**, 652–657 (2008).
- Choi, J. W. & Aurbach, D. Promise and reality of post-lithium-ion batteries with high energy densities. *Nat. Rev. Mater.* **1**, 16013 (2016).
- Li, W., Dahn, J. R. & Wainwright, D. S. Rechargeable lithium batteries with aqueous electrolytes. *Science* **264**, 1115–1118 (1994).
- Suo, L. et al. “Water-in-salt” electrolyte enables high-voltage aqueous lithium-ion chemistries. *Science* **350**, 938–943 (2015).
- Lin, M. C. et al. An ultrafast rechargeable aluminium-ion battery. *Nature* **520**, 325–328 (2015).
- Ponrouch, A., Frontera, C., Barde, F. & Palacin, M. R. Towards a calcium-based rechargeable battery. *Nat. Mater.* **15**, 169 (2015).
- Hassoun, J., Lee, K. S., Sun, Y. K. & Scrosati, B. An advanced lithium ion battery based on high performance electrode materials. *J. Am. Chem. Soc.* **133**, 3139–3143 (2011).
- Kim, H. et al. Aqueous rechargeable Li and Na ion batteries. *Chem. Rev.* **114**, 11788–11827 (2014).
- Kundu, D. et al. A high-capacity and long-life aqueous rechargeable zinc battery using a metal oxide intercalation cathode. *Nat. Energy* **1**, 16119 (2016).
- Pasta, M. et al. Full open-framework batteries for stationary energy storage. *Nat. Commun.* **5**, 3007 (2014).
- Pasta, M., Wessells, C. D., Huggins, R. A. & Cui, Y. A high-rate and long cycle life aqueous electrolyte battery for grid-scale energy storage. *Nat. Commun.* **3**, 1149 (2012).
- Lu, Y., Goodenough, J. B. & Kim, Y. Aqueous cathode for next-generation alkali-ion batteries. *J. Am. Chem. Soc.* **133**, 5756–5759 (2011).
- Wang, Y. et al. Ti-substituted tunnel-type Na_{0.44}MnO₂ oxide as a negative electrode for aqueous sodium-ion batteries. *Nat. Commun.* **6**, 6401 (2015).
- Yabuuchi, N., Kubota, K., Dahbi, M. & Komaba, S. Research development on sodium-ion batteries. *Chem. Rev.* **114**, 11636–11682 (2014).
- Su, D., McDonagh, A., Qiao, S. Z. & Wang, G. High-capacity aqueous potassium-ion batteries for large-scale energy storage. *Adv. Mater.* **29**, 1604007 (2017).
- Shan, X. et al. Bivalence Mn₅O₈ with hydroxylated interphase for high-voltage aqueous sodium-ion storage. *Nat. Commun.* **7**, 13370 (2016).
- Häupler, B. et al. Aqueous zinc-organic polymer battery with a high rate performance and long lifetime. *NPG Asia Mater.* **8**, e283 (2016).
- Sun, X. et al. Investigation of the mechanism of Mg insertion in birnessite in nonaqueous and aqueous rechargeable mg-ion batteries. *Chem. Mater.* **28**, 534–542 (2016).
- Bucur, C. B., Gregory, T., Oliver, A. G. & Muldoon, J. Confession of a magnesium battery. *J. Phys. Chem. Lett.* **6**, 3578–3591 (2015).

20. González, M. A. et al. Layered double hydroxides as a suitable substrate to improve the efficiency of Zn anode in neutral pH Zn-ion batteries. *Electrochem. Commun.* **68**, 1–4 (2016).
21. Trócoli, R. & La Mantia, F. An aqueous zinc-ion battery based on copper hexacyanoferrate. *ChemSusChem*. **8**, 481–485 (2015).
22. Tahil, W. The zinc air battery and the zinc economy: A virtuous circle. Available at: www.meridian-int-res.com/Projects/The_Zinc_Air_Solution.pdf (Meridian International Research, 2007).
23. Chamoun, M. et al. Hyper-dendritic nanoporous zinc foam anodes. *NPG Asia Mater* **7**, e178 (2015).
24. Zhang, N. et al. Cation-deficient spinel ZnMn_2O_4 cathode in $\text{Zn}(\text{CF}_3\text{SO}_3)_2$ electrolyte for rechargeable aqueous Zn-ion battery. *J. Am. Chem. Soc.* **138**, 12894–12901 (2016).
25. Cheng, Y. et al. Highly reversible zinc-ion intercalation into chevrel phase Mo_6S_8 nanocubes and applications for advanced zinc-ion batteries. *ACS Appl. Mater. Interfaces* **8**, 13673–13677 (2016).
26. Linden, D. & Reddy, T. *Handbook of Batteries* 3rd edn (McGraw-Hill, 2002).
27. Winter, M. & Brodd, R. J. What are batteries, fuel cells, and supercapacitors? *Chem. Rev.* **104**, 4245–4270 (2004).
28. Cheng, F. Y., Chen, J., Gou, X. L. & Shen, P. W. High-power alkaline Zn–MnO₂ batteries using γ -MnO₂ nanowires/nanotubes and electrolytic zinc powder. *Adv. Mater.* **17**, 2753–2756 (2005).
29. Kannan, A. M. et al. Characterization of the bismuth-modified manganese dioxide cathodes in rechargeable alkaline cells. *J. Electrochem. Soc.* **149**, A483 (2002).
30. McLarnon, F. R. & Cairns, E. J. The secondary alkaline zinc electrode. *J. Electrochem. Soc.* **138**, 645–656 (1991).
31. Shen, Y. & Kordesch, K. The mechanism of capacity fade of rechargeable alkaline manganese dioxide zinc cells. *J. Power Sources* **87**, 162–166 (2000).
32. Gibson, A. J. et al. Dynamic electrodeposition of manganese dioxide: Temporal variation in the electrodeposition mechanism. *J. Electrochem. Soc.* **163**, H305–H312 (2016).
33. Xu, C., Li, B., Du, H. & Kang, F. Energetic zinc ion chemistry: The rechargeable zinc ion battery. *Angew. Chem. Int. Ed.* **51**, 933–935 (2012).
34. Alfaruqi, M. H. et al. Electrochemically induced structural transformation in a γ -MnO₂ cathode of a high capacity zinc-ion battery system. *Chem. Mater.* **27**, 3609–3620 (2015).
35. Pan, H. et al. Reversible aqueous zinc/manganese oxide energy storage from conversion reactions. *Nat. Energy* **1**, 16039 (2016).
36. Lee, B. et al. Elucidating the intercalation mechanism of zinc ions into small alpha-MnO₂ for rechargeable zinc batteries. *Chem. Commun.* **51**, 9265–9268 (2015).
37. Lee, J. et al. Todorokite-type MnO₂ as a zinc-ion intercalating material. *Electrochim. Acta* **112**, 138–143 (2013).
38. Lee, B. et al. Electrochemically-induced reversible transition from the tunneled to layered polymorphs of manganese dioxide. *Sci. Rep.* **4**, 6066 (2014).
39. Yuan, Y. et al. The influence of large cations on the electrochemical properties of tunnel-structured metal oxides. *Nat. Commun.* **7**, 13374 (2016).
40. Jiao, F. & Bruce, P. G. Mesoporous crystalline β -MnO₂—a reversible positive electrode for rechargeable lithium batteries. *Adv. Mater.* **19**, 657–660 (2007).
41. Tompsett, D. A., Parker, S. C. & Islam, M. S. Rutile (β -)MnO₂ surfaces and vacancy formation for high electrochemical and catalytic performance. *J. Am. Chem. Soc.* **136**, 1418–1426 (2014).
42. Wei, C. et al. Preparation and characterization of manganese dioxides with nano-sized tunnel structures for zinc ion storage. *J. Phys. Chem. Solids* **73**, 1487–1491 (2012).
43. Yamada, A. et al. Room-temperature miscibility gap in Li_xFePO_4 . *Nat. Mater.* **5**, 357–360 (2006).
44. Luo, J. et al. Double-aging method for preparation of stabilized Na–buserite and transformations to todorokites incorporated with various metals. *Inorg. Chem.* **38**, 6106–6113 (1999).
45. Post, J. E. Manganese oxide minerals: Crystal structures and economic and environmental significance. *Proc. Natl Acad. Sci.* **96**, 3447–3454 (1999).
46. Golden, D. C., Chen, C. C. & Dixon, J. B. Transformation of birnessite to buserite, todorokite, and manganite under mild hydrothermal treatment. *Clays Clay Miner* **35**, 271–280 (1987).
47. Tepavcevic, S. et al. Nanostructured bilayered vanadium oxide electrodes for rechargeable sodium-ion batteries. *ACS Nano* **6**, 530–538 (2012).
48. Hu, Y. Y. et al. Origin of additional capacities in metal oxide lithium-ion battery electrodes. *Nat. Mater.* **12**, 1130–1136 (2013).
49. Lu, J. et al. Effectively suppressing dissolution of manganese from spinel lithium manganate via a nanoscale surface-doping approach. *Nat. Commun.* **5**, 5693 (2014).
50. Kim, C. et al. Direct observation of reversible magnesium ion intercalation into a spinel oxide host. *Adv. Mater.* **27**, 3377–3384 (2015).
51. Zhang, R. et al. α -MnO₂ as a cathode material for rechargeable Mg batteries. *Electrochem. Commun.* **23**, 110–113 (2012).
52. Li, C. et al. Phase and composition controllable synthesis of cobalt manganese spinel nanoparticles towards efficient oxygen electrocatalysis. *Nat. Commun.* **6**, 7345 (2015).
53. Thackeray, M. M. et al. Structural fatigue in spinel electrodes in high voltage (4 V) Li/Li_xMn₂O₄ cells. *Electrochem. Solid-State Lett.* **1**, 7–9 (1998).
54. Nam, K. W., Kim, M. G. & Kim, K. B. In situ Mn K-edge x-ray absorption spectroscopy studies of electrodeposited manganese oxide films for electrochemical capacitors. *J. Phys. Chem. C* **111**, 749–758 (2007).
55. Alfaruqi, M. H. et al. A layered δ -MnO₂ nanoflake cathode with high zinc-storage capacities for eco-friendly battery applications. *Electrochem. Commun.* **60**, 121–125 (2015).
56. Ramanujapuram, A. et al. Degradation and stabilization of lithium cobalt oxide in aqueous electrolytes. *Energy Environ. Sci.* **9**, 1841–1848 (2016).
57. Zhang, L., Chen, L., Zhou, X. & Liu, Z. Towards high-voltage aqueous metal-ion batteries beyond 1.5 V: The zinc/zinc hexacyanoferrate system. *Adv. Energy Mater.* **5**, 1400930 (2015).
58. Luo, J. Y., Cui, W. J., He, P. & Xia, Y. Y. Raising the cycling stability of aqueous lithium-ion batteries by eliminating oxygen in the electrolyte. *Nat. Chem.* **2**, 760–765 (2010).
59. Li, Z. et al. Towards high power high energy aqueous sodium-ion batteries: The NaTi₂(PO₄)₃/Na_{0.44}MnO₂ system. *Adv. Energy Mater.* **3**, 290–294 (2013).
60. Chandak, H., Sarode, P. & Bahekar, S. Zn(OTf)₂-mediated expeditious and solvent-free synthesis of propargylamines via C–H activation of phenylacetylene. *Synlett* **27**, 2209–2212 (2016).
61. Cheng, F. et al. Facile controlled synthesis of MnO₂ nanostructures of novel shapes and their application in batteries. *Inorg. Chem.* **45**, 2038–2044 (2006).
62. Yu, H. et al. The XAFS beamline of SSRF. *Nucl. Sci. Tech.* **26**, 050102 (2015).

Acknowledgements

This work was supported by MOST (2016YFA0202500 and 2017YFA0206702), NSFC (21231005, 21473235, and 11227902) and MOE (B12015, ACET-13-0296, and IRT13R30).

Author contributions

N.Z., J.L., and L.W. conducted the synthesis. N.Z. carried out the characterization and the electrochemical measurements. N.Z., F.C., and J.C. co-wrote the manuscript. N.Z., F.C., and X.L. analyzed the results of synchrotron X-ray absorption spectroscopy. All authors discussed the data and commented on the manuscript. F.C. and J.C. directed the research.

Additional information

Supplementary Information accompanies this paper at doi:10.1038/s41467-017-00467-x.

Competing interests: The authors declare no competing financial interests.

Reprints and permission information is available online at <http://npg.nature.com/reprintsandpermissions/>

Publisher's note: Springer Nature remains neutral with regard to jurisdictional claims in published maps and institutional affiliations.



Open Access This article is licensed under a Creative Commons Attribution 4.0 International License, which permits use, sharing, adaptation, distribution and reproduction in any medium or format, as long as you give appropriate credit to the original author(s) and the source, provide a link to the Creative Commons license, and indicate if changes were made. The images or other third party material in this article are included in the article's Creative Commons license, unless indicated otherwise in a credit line to the material. If material is not included in the article's Creative Commons license and your intended use is not permitted by statutory regulation or exceeds the permitted use, you will need to obtain permission directly from the copyright holder. To view a copy of this license, visit <http://creativecommons.org/licenses/by/4.0/>.

© The Author(s) 2017